Identification of Lagrangian Coherent Structures around Swimming Jellyfish from Experimental Time-series Data

Senior Thesis in Control and Dynamical Systems by:

Zhonglin J. Zhang

Thesis Advisor:
Professor John Dabiri

June 6, 2008

Abstract

The unique body kinematics of jellyfish embodies the most intriguing form of biological propulsion, which makes jellyfish a promising resource for developing new locomotion systems. Instead of the conventional Eulerian method, we take an unprecedented Lagrangian approach by tracking individual fluid particles around a swimming jellyfish over a finite time interval. Specifically, we utilize the Lagrangian coherent structures (LCS) in the flow field to investigate the flow characteristics around a jellyfish. LCS are separatrices or invariant manifolds, which separate the flow field into distinct regions. To locate the LCS in the flow, we employ the concept of the finite-time Lyapunov Exponent (FTLE), which measures the rate at which particles diverge from each other, and LCS are identified as the high-value ridges in the FTLE field. This method is implemented and validated by analysis on two-dimensional vortex dipole flow, two-dimensional experimental time-series data, and Hill's vortex sphere. This method is expected to extract LCS from three-dimensional experimental time-series data.

Table of Contents

List of Figures . . . . . **ii**

1 Introduction **1**
1.1 Background 1
1.2 The Lagrangian Coherent Structures 2
1.3 Existing Application of Lagrangian Coherent Structures 3
1.3.1 Monterey Bay Ocean Current 3
1.3.2 Flow Over An Airfoil 4

2 Technical Approach **6**
2.1 Experimental Setup 6
2.1.1 Potential Flow Models 6
2.1.2 Flow Measurement by Particle Tracking 8
2.2 Analytical Methods 9
2.2.1 Finite-time Lyapunov Exponent (FTLE) 9
2.2.2 FTLE Approximation with Gaussian Weight 11
2.3 Implementation: The Graphical User Interface 13

3 Results and Discussion **15**
3.1 Two-dimensional Steady Flow: Vortex Dipole 15
3.1.1 Comparing the FTLE field: The Norm Method 15
3.2 Three-dimensional Steady Flow: Hill's Vortex Dipole 19
3.3 Two-dimensional Unsteady Flow: Flow around Jellyfish 22
3.3.1 Particle Density Normalization 24

4 Conclusion and Future Work **27**

Acknowledgements **28**

Bibliography **29**

List of Figures

Figure 1.1 This picture shows *Aurelia aurita*, also known as moon jellyfish, swimming via full body undulations that create vortex rings of alternating rotational orientation during the swimming cycle. **1**

Figure 1.2 These pictures illustrate how two points on either side of invariant manifold will diverge from each other a finite time interval. **3**

Figure 1.3 These pictures illustrate the velocity field and the corresponding forward-time FTLE field around Monterey Bay measured by CODAR. **4**

Figure 1.4 These pictures illustrate the velocity field and the corresponding forward-time FTLE field over a GLAS-II airfoil. **5**

Figure 2.1 This figure plots the streamlines and the velocity field of vortex dipole flow and Hill's vortex sphere. **7**

Figure 2.2 This figure illustrates how Lagrangian particles are deployed in around a swimming jellyfish. **8**

Figure 2.3 This figure illustrates a reference particle trajectory, the adjacent trajectory and the displacement vector between them. **10**

Figure 2.4 This diagram illustrates how the algorithm computes the FTLE value at a specific Eulerian grid point. **12**

Figure 2.5 This pictures shows the outlook the of the graphical user interface that is implemented to calculate FTLE field from particle trajectory data. **13**

Figure 3.1 These figures plot the forward-time and backward-time FTLE field of a vortex dipole flow at different times. **16**

Figure 3.2 This figure illustrates the Lagrangian particles in a vortex dipole flow. **17**

Figure 3.3 These figures plot the forward-time FTLE field of a vortex dipole flow with different tracer densities. **17**

Figure 3.4 The norm of the FTLE field plotted against the particle density for the two-dimensional vortex flow model. **18**

Figure 3.5 Forward-time FTLE field for a vortex dipole flow with random initial tracer distribution. **19**

Figure 3.6 This figure plots the three-dimensional positions of the tracer particles around a vortex sphere at different time frames. **20**

Figure 3.7 These figures plot the forward-time FTLE field of a spherical vortex flow with different tracer densities. **20**

Figure 3.8 The norm of the FTLE field plotted against the particle density for the three-dimensional vortex flow model. **21**

Figure 3.9 This figure plots the velocity field from a previous PDIV measurement at various time frames. Tracer particles are seeded in the flow field and plotted on top of the velocity field. **22**

Figure 3.10 This figure plots the forward-time and backward-time FTLE field from a previous PDIV measurement at various time frames. **23**

Figure 3.11 This figure plots the forward-time and backward-time FTLE field from a previous PDIV measurement at various time frames. **25**

Figure 3.12 The norm of the FTLE field is plotted against the particle density for the flow around a jellyfish; the normalized FTLE norm is also plotted against the normalized particle density in this figure as well. **25**

Figure 3.13 This figure plots the backward-time FTLE field with a short tracking time at different time frames. **26**

Chapter 1

Introduction

1.1 Background

Jellyfish form a vital component of ocean ecology and also preserve one of the most ancient forms of biological propulsion (Figure 1.1). Their simple anatomy and body kinematics make them a promising candidate for studies aiming to discover new locomotion systems. Empirical observations and theoretical modeling have demonstrated that jellyfish use the formation and shedding of vortices to move and capture preys. In fact, much of the experimental work on jellyfish swimming has been approached from a perspective of the vorticity dynamics around the jellyfish [8].

Figure 1.1 *Aurelia aurita*, also known as moon jellyfish, swims via full body undulations that create vortex rings of alternating rotational orientation during the swimming cycle.

Increasingly, many dynamical systems, such as the flow field around a jellyfish, are determined not by analytically defined model systems, but by data from experiments or large-scale simulations. In the past, analyses on fluid flow have been performed primarily in the Eulerian frame, in which measurements are taken at fixed locations in space. The standard tool for flow field measurements is digital particle image velocimetry (DPIV), which quantifies the velocity field of the flow in an Eulerian frame of reference. To compute the instantaneous force and moment created by the swimming animal, the calculation of the vorticity field is needed [7]. Although the vorticity field can be simply deduced by taking the curl of the velocity field, the vorticity dynamics around swimming animals, with the exception of a steady flow, involves either measurement of the boundary layers on the animal, replacement of animal body with

equivalent system of vortex sources, or measurements on the surface of a control volume with length scales an order of magnitude larger than the animal itself [8]. In principle, the calculation of flow dynamics around the boundary layer is a rather time-consuming process, and the vorticity field usually cannot be well resolved at the interface between the animal and the surrounding water while maintaining a full-field view of the flow [2]. The large domain size required by the control volume also prolongs the overall computation. All of these conditions set restraints on the Eulerian approach to the animal swimming problem.

1.2 The Lagrangian Coherent Structures

In light of these limitations, it is clear that an alternative approach is necessary. The major challenges presented in the Eulerian method lie in the need to identify consistent boundaries in the flow field on which to evaluate the equation of motion. The boundaries of the control volume consist of either the fluid-solid boundary represented by the animal surface or a virtual, fluid-fluid boundary around the swimming animal [8]. The former boundary can be easily identified given the geometry of the animal surface, and the latter case can be determined by an innovative technique, which is the central subject of this thesis project. Instead of the Eulerian approach, we take the Lagrangian perspective, tracking particles in the flow field to allow a more precise flow characterization than the traditional methods. Recent applications of similar Lagrangian analysis have demonstrated that there exist some virtual yet physically meaningful fluid-fluid boundaries in aperiodic flows [11], which are very common around many swimming animals. These boundaries are identified as Lagrangian coherent structures (LCS).

LCS is a concept originating in the study of dynamical systems. These coherent structures are generally known as invariant manifolds or separatrices [11] in the phase space of a time-dependent system. They mark the borders where no trajectories pass through, and therefore separate the flow field into dynamically distinct regions. To locate the LCS in the flow, we need to first employ the concept of the finite-time Lyapunov exponent (FTLE), which measures the rate at which particles diverge from each other at a given time and location. Intuitively, two particles can be traced along two adjacent trajectories for a finite time period, and the evolution of the displacement between the two particles can be evaluated. The FTLE is then computed from the ratio of the final displacement over the initial displacement [10]. Hence, particle trajectories will diverge at a location with a high FTLE value, and FTLE can be recognized as the degree of "stretchiness" of the flow field at a fixed point over a finite period of time. Furthermore, if particles are traced forward in time, the resulting FTLE value is called the forward-time FTLE. Similarly, tracing the trajectories backward in time will result in the backward-time FTLE. To calculate the LCS, we can obtain the FTLE field from the flow data and identify the ridges of high FTLE values as the LCS. Because of the time-dependent nature of FTLE values, LCS computed from the forward-time FTLE field is called the forward-time

LCS (fLCS) (or repelling LCS), and the backward-time FTLE field leads to reverse-time LCS (rLCS) (or attracting LCS) [8, 10].

Consider a generic hyperbolic point in a time-independent dynamical system and its associated stable and unstable manifolds (Figure 1.2). If we follow the trajectories of two points that are initially on either side of a stable manifold (at location A along the green and red trajectories) forward in time, then the two points will eventually diverge from each other. Likewise, if we start tracing two points on either side of an unstable manifold (at location B along the green and blue trajectories) backward in time, then the points will diverge from each other. Therefore, fLCS are the analogous stable manifolds which repel nearby trajectories for a time-dependent system; similarly, rLCS are the unstable manifolds that attract nearby trajectories in the flow field. The derivation of FTLE and the identification of the LCS in the flow field is a rather complicated process and is explained later in Chapter 2.

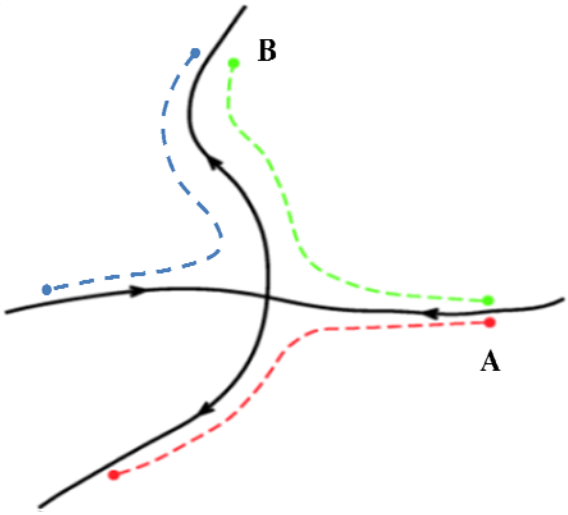

Figure 1.2 Two points from either side of the stable manifold (green and red trajectories) will diverge from each other if tracked forward in time; two points from either side of the unstable manifold (green and blue) will diverge from each other if tracked backward in time.

1.3 Existing Applications of Lagrangian Coherent Structures

1.3.1 Monterey Bay Ocean Current

The Lagrangian coherent structures (LCS) have been used primarily to better understand transport and mixing processes or to identify fluid structures in various kinds of flows. One interesting application of LCS is in the analysis of flow transport in the ocean. Although models of ocean currents have been studied for years, only simple analytical model or coarse flow measurements were available to marine biologist [6]. Fortunately, since the recent introduction of High Frequency Radar technology, which is often referred to as CODAR for COstal raDAR, high-resolution real-time ocean velocity measurements have become available (Figure 1.3). One location that CODAR has been installed is around Monterey Bay, California. Figure 1.3 (a) shows a snap shot of the CODAR velocity data during August 2003, and Figure 1.3 (b) shows the forward-time FTLE field obtained from the CODAR data at that particular moment. There is an LCS which extends across the mouth of the bay and forms an invisible boundary across the bay. Particles on the right of the LCS will stay inside the bay and re-circulate, while particles to the left of the LCS will continue down the California coast.

For marine biologists, this invisible boundary is extremely important because it controls the flow of water as well as pollutants. Near the middle of the bay, a power plant releasing warm waste water can raise the average temperature of the bay high enough to kill many native ocean animals. Depending on which side of the sewage pipe the boundary lies on, the waste water will either flow out to the sea, where its effect will be negligible or re-circulate into the bay and heat it up [6]. Hence, LCS allow scientists to model the complex flow of water in the bay and suggest a strategy for minimizing the damaging effects of the effluent from the power station.

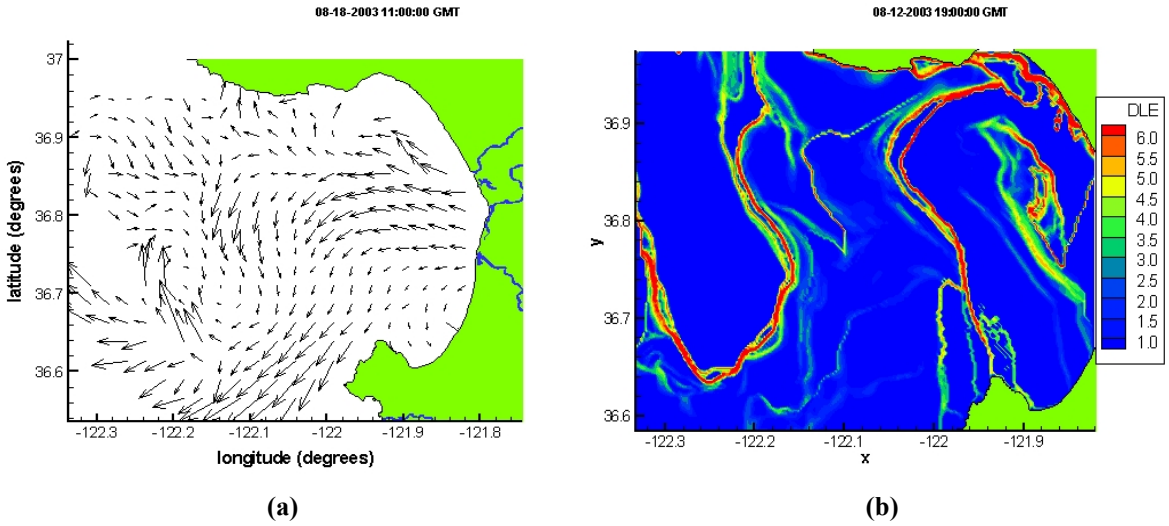

(a) **(b)**

Figure 1.3 The picture on the left (a) illustrates a snap shot of the velocity field around Monterey Bay measured by CODAR. The picture on the right (b) shows the corresponding forward-time FTLE field calculated from the given velocity field. The forward-time LCS can be identified as the red line crossing the bay vertically.

1.3.2 Flow Over An Airfoil

In addition, the application of LCS has been extended to the identification of unsteady separation profiles over airfoils. For most airplanes, flow separation over the wings leads to stall. Therefore, such behavior is very undesirable and airfoils are typically designed to avoid separation. However, recent developments in the field of aerodynamics have led to a new way of controlling air flow which actually induces separation over the top of an airfoil. An example of this is the GLAS-II airfoil [2] (Figure 1.4). This airfoil geometry has been used in the area of active flow control where an oscillatory blowing valve is placed on the surface of the airfoil to provide regulated pressure oscillations by means of blowing or suction. This enables control of the separation and many other aerodynamic properties such as lift and drag.

However, engineers have argued for years on how to even define separation. The only consensus is that flow separation involves the ejection of air along some path away from a surface. Therefore, the separation profile behaves like an unstable manifold that repels particles

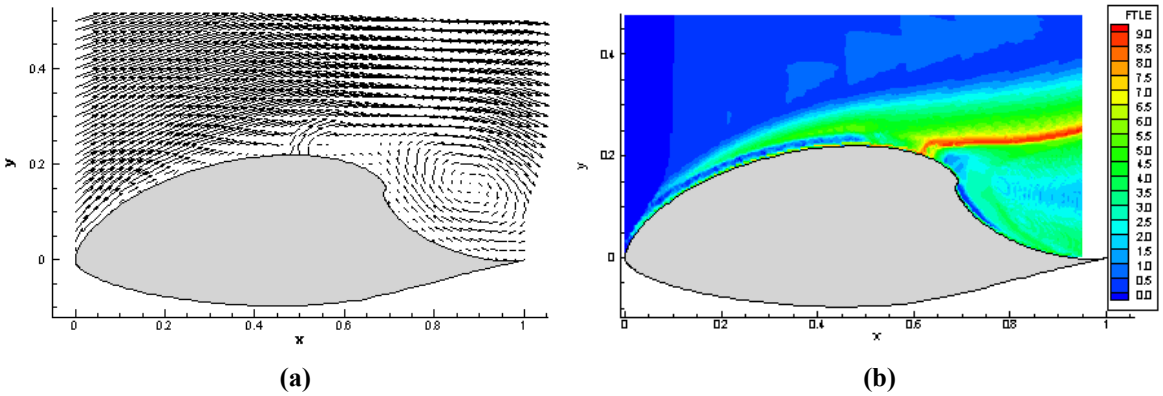

(a) **(b)**

Figure 1.4 The picture on the left (a) illustrates a snap shot of the velocity field around a GLAS-II airfoil. The picture on the right (b) shows the corresponding backward-time FTLE field calculated from the given velocity field. The backward-time LCS can be identified as the red line extending from the upper surface of the airfoil.

near the separation point. As previously mentioned, the region around an unstable manifold will generate high value ridges in the backward-time FTLE field. The velocity field for flow over a GLAS-II airfoil has been simulated by numerical methods and provided by Jeff Eldridge [2]. In Figure 1.4a, a snap shot of the simulated velocity field is shown, and the corresponding backward-time FTLE field is shown in Figure 1.4b. As we can see from the contour plot of the FTLE field, the backward-time LCS is highlighted as the red line in the flow field. Hence, given the exact location of the separation profile, aeronautical engineers can easily identify the separation point and control the flow.

Chapter 2

Technical Approach

2.1 Experimental Setup

2.1.1 Potential Flow Models

LCS have previously been used to analyze dynamical systems identified by highly dense experimental data, such as the CODAR measurements, and direct numerical simulations, such as the GLAS-II airfoil data, but have not been applied to biomechanical data, or any small scale experimental time-series data. Because there has not been any previous research on LCS identification in the Lagrangian framework, we are compelled to concentrate on a few intermediate steps before solving the three-dimensional LCS extraction problem. Therefore, we start with analysis of both planar and three-dimensional steady flow models.

Since jellyfish generate vortices underneath their bodies to propel upward, we first investigate a two-dimensional vortex flow to simulate the flow around a swimming jellyfish. In this case, the flow around a vortex dipole is simulated (Figure 2.1 (a)) and Lagrangian particles are distributed around the dipole. In this model, two vortex sources with equal but opposite vorticity strength are placed along the x-axis and equidistant from the origin. Lamb et al. (1932) provides the model for a potential flow around a vortex dipole in the Cartesian coordinate [7]:

$$u = \frac{\Gamma}{2\pi}\left(b + \frac{y}{(x-a)^2 + y^2} - \frac{y}{(x+a)^2 + y^2}\right) \tag{2.1}$$

$$v = -\frac{\Gamma}{2\pi}\left(\frac{1}{2a} + \frac{x-a}{(x-a)^2 + \mathrm{y}^2} - \frac{x+a}{(x+a)^2 + y^2}\right) \tag{2.2}$$

where u and v represent the x and y components of the velocity vector, respectively. a is the distance of the vortex sources from the origin. The strength of the vortex source pair is specified by Γ. Furthermore, in order to implement an algorithm that can be used on three-dimensional experimental data, Hill's vortex sphere is studied extensively during the course of the thesis

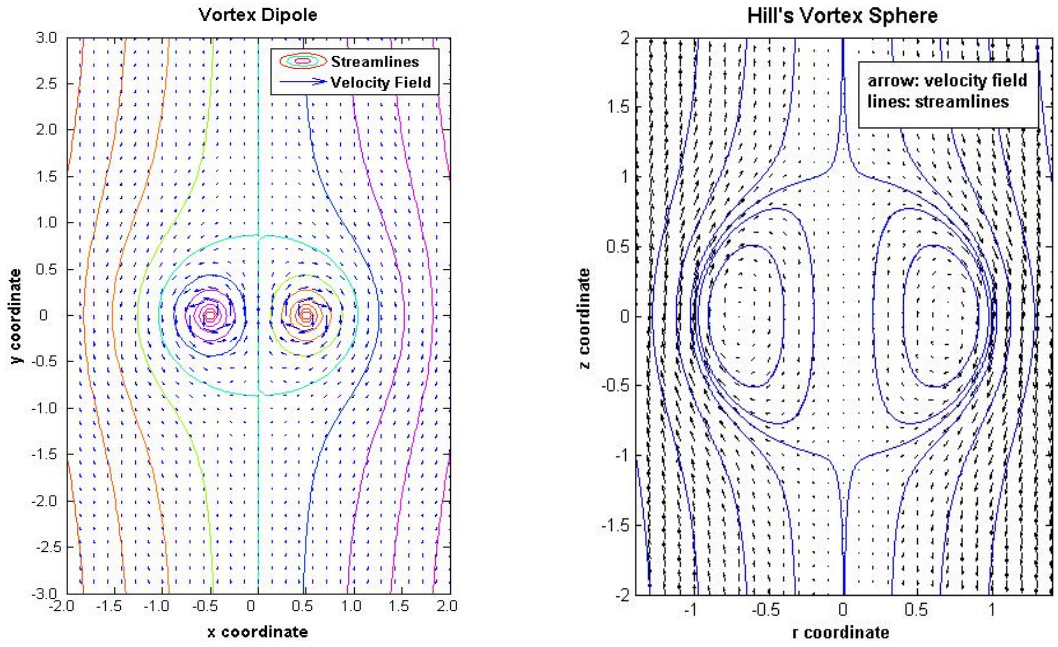

(a) **(b)**

Figure 2.1 The streamlines and the velocity field plots for (a) a vortex dipole flow and (b) Hill's vortex sphere. The separatrix for vortex dipole is highlighted as the cyan-colored ellipse and the separatrix for Hill's vortex sphere is a sphere centered on the origin with radius 1.

Figure 2.1 (b) shows the velocity field and several streamlines in the flow field. In this model, a uniform flow passing over a three-dimensional vortex dipole is simulated. The combination of the uniform flow speed and the vorticity strength of thedipole will determine the size of the vortex sphere. Peng et al. (2007) provides the model for this spherical vortex flow in the cylindrical coordinate system (r, θ, z) [8]. Since this flow model is asymmetric around the z-axis, the θ component of the velocity vector is zero:

$$\begin{cases} u_r = \dfrac{3}{2} Uz \left(\dfrac{r^2}{R^2} \right) \\ u_z = Ur \left(1 - \dfrac{z^2}{R^2} - \dfrac{2r^2}{R^2} \right) \end{cases} \qquad r^2 + z^2 \le R, \tag{2.3}$$

$$\begin{cases} u_r = \dfrac{3}{2} Uz \left[\dfrac{r^2 R^3}{(z^2 + r^2)^{5/2}} \right] \\ u_z = -\dfrac{1}{2} Ur \left[2 + \dfrac{R^3 (r^2 - 2z^2)}{(z^2 + r^2)^5} \right] \end{cases} \qquad r^2 + z^2 > R, \tag{2.4}$$

where u_r and u_z are the r and z components of the velocity vector, respectively. R equals to the radius of the sphere, and U is the speed of the external flow.

As the Lagrangian particles move along the trajectories given by the flow models, their positions over a time interval are tracked and used to compute the FTLE field in the specified domains. The resulting LCS can be compared with the analytical answer to these models. The results can also be used to answer these following questions: How many Lagrangian particles are required to provide a precise measurement of the LCS around a swimming animal? How long should the particles be tracked in order to reveal the LCS? And how frequently should we track the particles?

2.1.2 Flow Measurement by Particle Tracking

The answers to the these questions are vital to the design of an experiment currently conducted by the research group led by Professor John Dabiri from the Graduate Aeronautical Laboratory of California Institute of Technology (GALCIT). In this case, we are studying unsteady flow around jellyfish and the vortex rings generated beneath their bodies which force the surrounding prey within the reach of their tentacles.

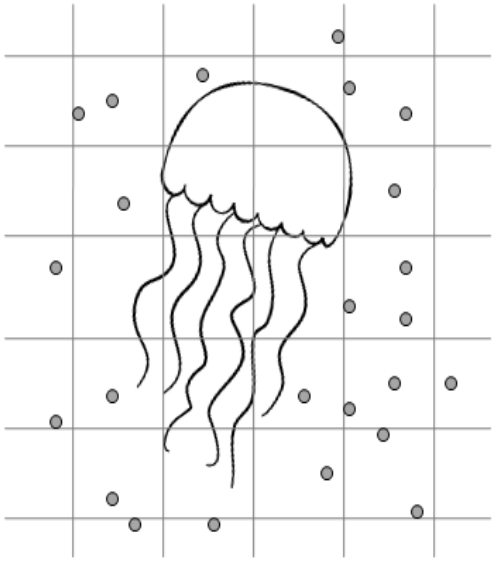

Figure 2.2 Lagrangian particles (small dark circles) are deployed around a jellyfish in a specified domain.

In the experiment, a large number of tracers are deployed in the flow around a swimming moon jellyfish (Figure 2.2). Defocusing Digital Particle Image Velocimetry (DDPIV), an extension of the planar DPIV technique to the third dimension [9], is used to measure three-dimensional positions of all particles over a finite time interval. The tracer particles used in the experiment are 14 micron (diameter) silver coated glass beads. Their low density allows them to suspend in water and minimize the gravitational effect on the particle velocity. The luminous nature of the glass beads also enhances the accuracy of the DDPIV measurements. However, these particles need to be tracked to obtain their corresponding trajectories. An algorithm called Polynomial Fitting with Gaussian Weight (PFGW) is used in the experiment to identify each tracer particle. This algorithm is designed to track the motion of low-contrast particles against a background with large variations in light levels. The method is based on a polynomial fit of the intensity around each tracked particle, weighted by a Gaussian function of the distance from the center [10]. It is especially suitable for tracking small and dense particles such as endogenous particles in the cell. The small size of the tracer particles, hence, further facilitates the performance of the tracking algorithm.

Conventionally, FTLE fields have been calculated from the velocity field measurements typically taken by DPIV in an Eulerian frame [3, 5, 8]. However, the Lagrangian method introduced in this thesis computes the FTLE field from a time-series of particle trajectories. The data output of this experiment consist of three-dimensional trajectories in the flow field and their

tracking indices. The resulting FTLE field will reveal surface-like coherent structures that separate the flow field into distinct regions. If the conventional Eulerian method were to be adapted, the computation of FTLE field from the full three-dimensional velocity field would require lengthy integrations of each particle trajectory. Consequently, it would take days to complete the computation for the three-dimensional FTLE field at just one time frame. In contrast, in the Lagrangian approach, the position of each particle is measured over time. The FTLE value at a given point would be obtained from the change of distance between two close-by particles over that time interval. The distance between any pair of adjacent particles at the specified time frame can be conveniently calculated by retrieving their positions. Therefore, the Lagrangian method simplifies the FTLE computation by avoiding the most time-consuming process (i.e. integration of particle trajectories) and significantly reduces the overall run time. Although this method is computationally inexpensive, compared to the dense velocity field data, the particle trajectory data are rather sparse. In parts of the flow field where Lagrangian particles are unavailable, this method simply cannot provide enough information to deduce the FTLE value. Yet, despite the limited abundance of prey particles, the measured data is sufficient to obtain the local maxima in the FTLE field, thus revealing the LCS in the flow field. Chapter 3 will provide additional detail discussion about the results obtained by the Lagrangian method.

2.2 Analytical Methods

2.2.1 Finite-time Lyapunov Exponent (FTLE)

By tracking each Lagrangian particle in the flow over a finite period of time, the position of each particle along a trajectory at any time in that interval is given. A flow map can be used to map fluid particles from their initial positions at time t_0 to their locations after a finite time interval T at t_0+T. If the initial position of a particular particle at t_0 is given as $\mathbf{x}(t_0) = \mathbf{x}_0$, the particle after a time interval T can be tracked by the flow map,

$$\phi_{t_0}^{t_0+T}(x) : \mathbf{x}(t_0) \mapsto \mathbf{x}(t_0 + T). \tag{2.5}$$

We use $\mathbf{x}(t) = \phi_{t_0}^{t}(\mathbf{x}_0)$ to represent particle trajectory with initial condition $\mathbf{x}_0$ as a function of time t. Assume a trajectory starts slightly away from a reference trajectory $\mathbf{x}(t)$, with a small perturbed initial position $\mathbf{x}_0 + \delta\mathbf{x}_0$ at time t_0, this trajectory will evolve with a vector displacement

$$\delta\mathbf{x}(t) = \phi_{t_0}^{t}(\mathbf{x}_0 + \delta\mathbf{x}_0) - \phi_{t_0}^{t}(\mathbf{x}_0), \tag{2.6}$$

with respect to the reference trajectory $\mathbf{x}(t)$, as illustrated in Figure 2.3.

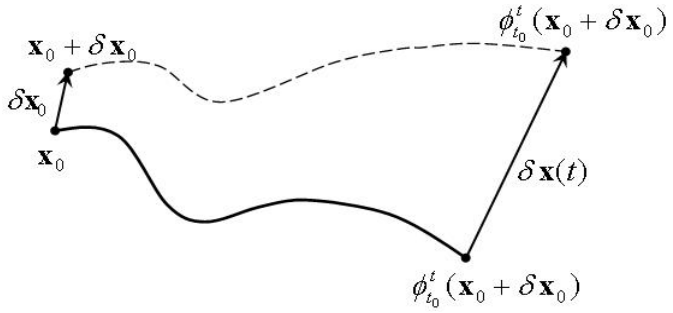

Figure 2.3 This figure illustrates the reference trajectory $\boldsymbol{\phi_{t_0}^{t}(\mathbf{x}_0)}$, the adjacent trajectory $\boldsymbol{\phi_{t_0}^{t}(\mathbf{x}_0 + \delta\mathbf{x}_0)}$, and the displacement vector between them $\boldsymbol{\delta\mathbf{x}(t)}$.

To quantify the linear transformation between the initial and the final displacement vectors, we can linearize the flow map around $\delta\mathbf{x}_0$ by expanding Equation 2.6 in a Taylor series and dropping the high order terms to yield:

$$\delta\mathbf{x}(t) = \frac{\partial\phi_{t_0}^{t}(\mathbf{x}_0)}{\partial\mathbf{x}_0}\delta\mathbf{x}_0. \tag{2.7}$$

The resulting first-order factor $\frac{\partial\phi_{t_0}^{t}(\mathbf{x_0})}{\partial\mathbf{x_0}}$ is the state-transition matrix, which can also be called the deformation gradient tensor, usually denoted by $\nabla\phi_{t_0}^{t}(\mathbf{x}_0)$ [12]. This matrix contains information about the expansion, contraction, and rotation of the initial displacement vector due to the deforming nature of the flow around $\mathbf{x}_0$. The magnitude of the final displacement vector can be obtained by taking the norm of the following inner product:

$$\begin{aligned}\|\delta\mathbf{x}(t)\| = \sqrt{\delta\mathbf{x}(t)^{*}\delta\mathbf{x}(t)} &= \sqrt{\left(\nabla\phi_{t_0}^{t}(\mathbf{x}_0)\delta\mathbf{x}_0\right)^{*}\left(\nabla\phi_{t_0}^{t}(\mathbf{x}_0)\delta\mathbf{x}_0\right)} \\ &= \sqrt{\delta\mathbf{x}_0{}^{*}\left[\nabla\phi_{t_0}^{t}(\mathbf{x}_0)^{*}\nabla\phi_{t_0}^{t}(\mathbf{x}_0)\right]\delta\mathbf{x}_0}\,.\end{aligned} \tag{2.8}$$

In the above expression, the symmetric matrix

$$\Delta = \nabla\phi_{t_0}^{t}(\mathbf{x}_0)^{*}\nabla\phi_{t_0}^{t}(\mathbf{x}_0) \tag{2.9}$$

is the finite-time right Cauchy-Green deformation tensor [12]. The matrix Δ is a rotation-independent measure of deformation [11]. Since Δ is an *n*-dimenstional, symmetric, and positive definite matrix, it has *n* real, positive eigenvalues [13, 14]. In addition, because our study focuses on 3-dimensional flow field, all vectors and matrices discussed in this paper are assumed to be 3-dimensional ($n = 3$).

Let $\lambda_{max}(\Delta)$ be the maximum eigenvalue of the Cauchy-Green tensor. From Equation 2.8 and 2.9, it can be deduced that $\sqrt{\lambda_{max}(\Delta)}$ represents how much the initial displacement vector $\delta\mathbf{x}_0$ can be stretched at time *t,* if $\delta\mathbf{x}_0$ is aligned with the eigenvector associated with $\lambda_{max}(\Delta)$. The final displacement vector, therefore, has maximum magnitude equal to

$$\|\delta\mathbf{x}(t)\|_{max} = \sqrt{\delta\mathbf{x}_0{}^*\ \lambda_{max}(\Delta)\ \delta\mathbf{x}_0} = \sqrt{\lambda_{max}(\Delta)}\|\delta\mathbf{x}_0\|. \tag{2.10}$$

We can further relate the flow field at $\mathbf{x}(t_0)$ to a finite-time Lyapunov exponent, defined as

$$\sigma_{t_0}^{t} = \frac{1}{|T|}\log\sqrt{\lambda_{max}(\Delta)} = \frac{1}{|T|}\log\left\|\frac{\delta\mathbf{x}(t)}{\delta\mathbf{x}(t_0)}\right\|, \tag{2.11}$$

where $T = t - t_0$ is the finite time duration over which deformation is measured. As previously mentioned, the finite-time Lyapunov exponent (FTLE) provides a measure that quantifies how trajectories diverge from each other at a particular position in a flow field. In other words, if $\delta\mathbf{x}_0$ is aligned with the eigenvector associated with $\lambda_{max}(\Delta)$, then the maximum stretching $\|\delta\mathbf{x}(t)\|$ of the displacement vector occurring from t_0 to $t = t_0 + T$ can be derived from Equation 2.11:

$$\|\delta\mathbf{x}(t)\| = e^{|T|\sigma_{t_0}^{t}}\|\delta\mathbf{x}_0\|. \tag{2.12}$$

Namely, $\sigma_{t_0}^{t}$ is called the finite-time Lyapunov exponent because it represents the exponent of the stretching factor $e^{|T|\sigma_{t_0}^{t}}$ that quantifies the transformation between the initial and final displacement vector.

Taking $T>0$, the local maxima in the FTLE field indicate the locally maximum trajectory divergence in the flow field; particle trajectories tend to repelled from these locations. If these local maxima merge together and form into ridges, these ridges then act as high impedance barriers in the flow field where no particle pass through. As discussed previously, these ridges are the forward-time Lagrangian coherent structures (LCS). Similarly, taking $T<0$, the high FTLE value ridges will reveal the backword-time LCS [12]. According to Shadden et al. (2005) and Peng et al. (2007), the estimated fluid flux across an LCS is, in fact, negligible. Hence, the LCS can be indeed treated as ideal material lines in the flow field.

2.2.2 FTLE Approximation with Gaussian Weight

To calculate the FTLE field, a non-inertial Eulerian frame is laid over the flow field around the swimming animal as shown in Figure 2.4. At each grid in this steady frame, the nearby Lagrangian particles are located within a searching range r_0, which is determined by the average particle density of the entire flow field. The positions of all possible combinations of particle

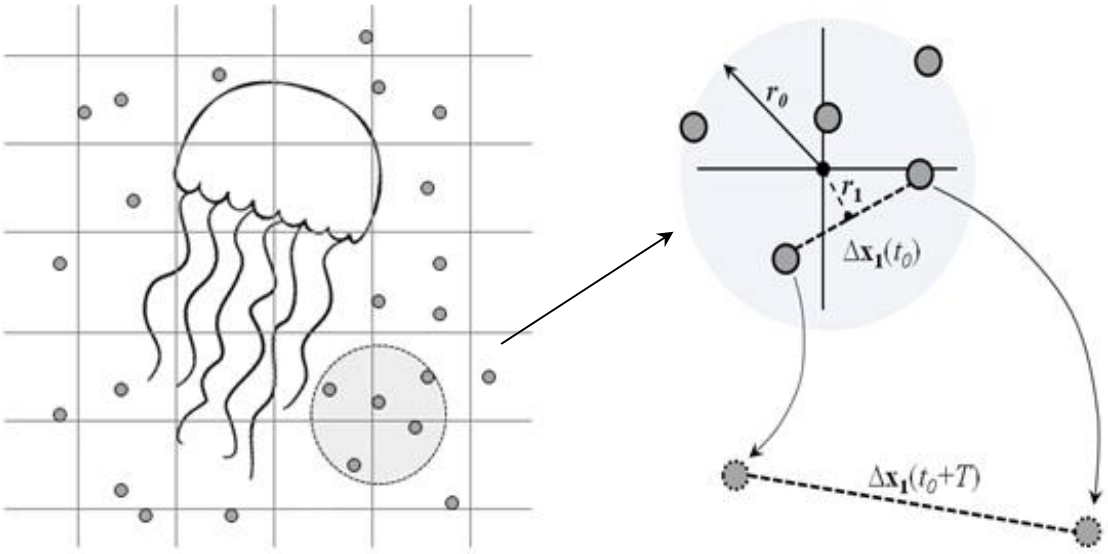

Figure 2.4 This diagram illustrates the algorithm that computes the FTLE value at a specific Eulerian grid point (left). The grid size and the searching range in the diagram are not drawn to scale relative to the size of the illustrated jellyfish. The searching range is defined by r_0, and r_1 is the distance between the Eulerian grid point and the midpoint of the first traced particle pair (right).

pairs are tracked over a time interval T. For each pair of tracers i, the corresponding FTLE is calculated from the following expression, similar to Equation 2.11:

$$\sigma_i = \frac{1}{|T|} \log \left\| \frac{\Delta \mathbf{x}_i(t_0 + T)}{\Delta \mathbf{x}_i(t_0)} \right\| \tag{2.13}$$

As shown in Figure 2.4, T is the finite time interval, and $\Delta \mathbf{x}_i(t_0)$ and $\Delta \mathbf{x}_i(t_0 + T)$ represent the initial and final displacement vectors between the pair of particles, respectively. Furthermore, a probability factor p_i is assigned to the corresponding particle pair i, according to the following:

$$p_i = \exp\left(-\frac{3\, r_i^2}{r_0^2}\right) \tag{2.14}$$

where r_0 is the searching range, and r_i symbolizes the distance between the specified Eulerian grid and the midpoint of the pair of particles. Hence,

$$\sigma_{x_0, y_0} = \frac{\Sigma p_i \sigma_i}{\Sigma p_i} \tag{2.15}$$

gives an estimate of the FTLE field at the grid point (x_0, y_0). In this equation, the collective FTLE contributions from all combinations of particle pairs around (x_0, y_0) is divided by the sum of the corresponding probability factors to give the "expected value" of the FTLE field at the given grid point. Considering Equation 2.14, which is simply a variation of the Gaussian distribution, Equation 2.15 implies that the pair with a midpoint closer to the grid point would have a greater contribution towards the overall FTLE value at the grid point. However, this algorithm provides an estimation of the FTLE value at each grid point based on the trajectory divergence of the surrounding particles. Although this method cannot provide exact FTLE value at each grid, the "expected value" of FTLE is sufficient to reveal the high-valued ridges, thus identifying the LCS in the flow field.

2.3 Implementation: The Graphical User Interface

Figure 2.5 The picture shows the outlook of the graphical user interface design that is developed by the author. With this software package, people with different background are able to use the algorithm described in the previous section.

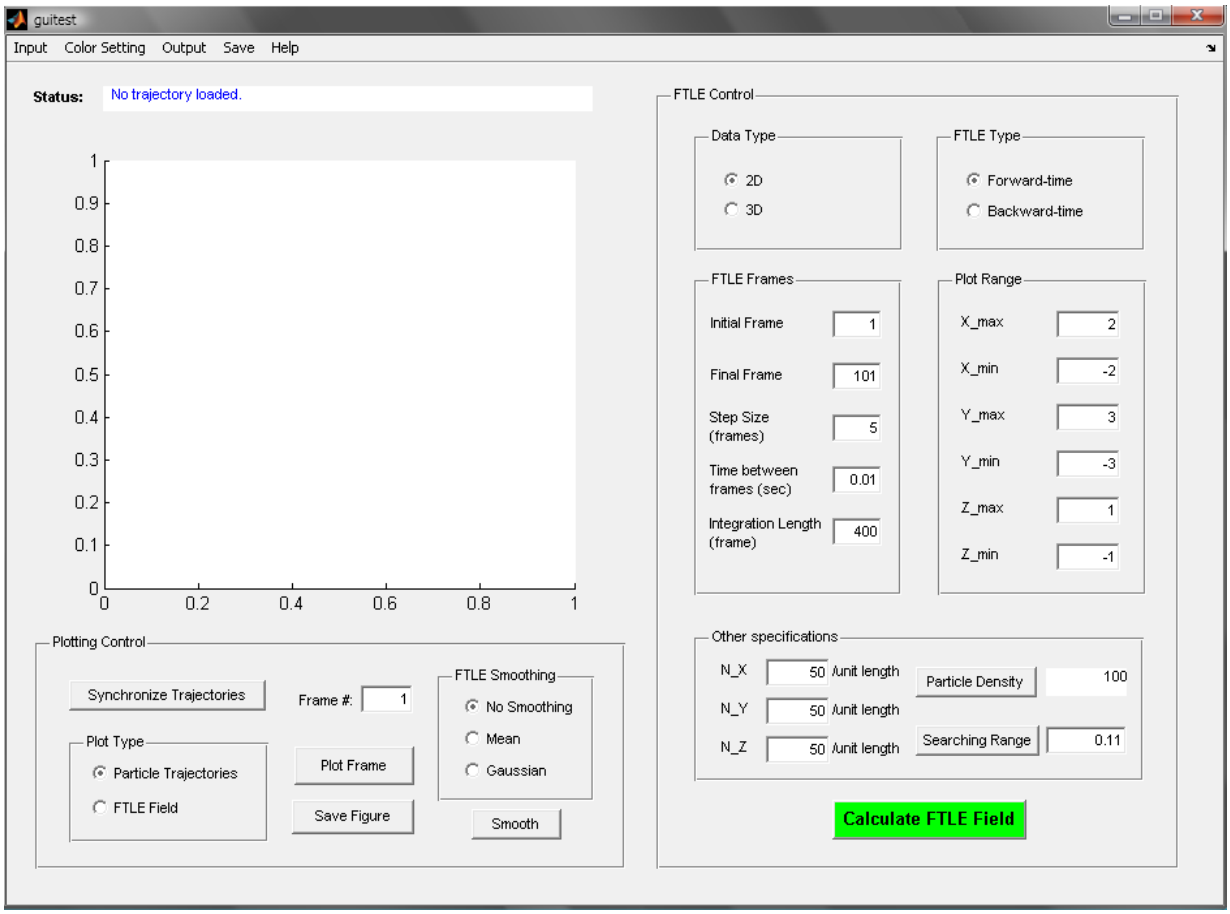

In an attempt to implement the algorithm described in Chapter 2.2, the author developed a software package that computes FTLE field of a specific region from a time-series trajectory data set. The software package is a MATLAB graphical user interface (GUI) which is designed to facilitate future experiments on animal swimming and provide a visual platform that people from different fields can access.

Figure 2.5 illustrates the outlook of the GUI program. The GUI is divided into two main portions. The part on the right allows the users to specify various conditions for FTLE calculation such as the grid size, data type, integration length, searching range etc. The part on the right allows the users to determine the type of plot to appear on the screen. Once the data is loaded into the program, the users can plot either the particle trajectory or the calculated FTLE field. The text bar on top of the plotting region will show the current status of the GUI, whether it is loading the trajectory or calculating the FTLE field. Furthermore, by using the menu bar on the top, the users have the options to load experimental data, save the analysis results, change the colormap of the contour plot, and many other functions. The input data format for this GUI program is the coordinate of the tracer particles followed by the particle index and time frame label. Due to the inevitable tracking error, not every particle's position is tracked in all time frames. The missing trajectory data will be approximated by cubic interpolation, which is implemented in the "Synchronize Trajectories" push button command.

However, this algorithm does not include the calculations of the LCS splines from FTLE fields, the procedure that can be accomplished by a variety of informal methods including thresholding or graphical feature extraction. Although rigorous methods have been implemented in the past [3~5], for practical purposes, identification of LCS from well-resolved FTLE fields is relatively insensitive to the current implemented method [12]. Furthermore, since MATLAB is not the most efficient programming language, a significant improvement on the performance will be expected if the GUI is written in other programming language such as C or C++.

Chapter 3

Results and Discussion

3.1 Two Dimensional Steady Flow: Vortex Dipole

First, in order to verify the current algorithm, we concentrated on investigating the case of planar flow around a vortex dipole. Figure 3.1 (a) shows the forward-time FTLE field calculated from the position data of the Lagrangian particles at $t = 1$; (c) shows the corresponding backward-time FTLE field of the vortex dipole flow; (b) and (d) plot the corresponding FTLE field at after 39 time steps. The Lagrangian particles in this case start at lattice grid points with 0.1 unit spacing. The FTLE field plots at $t = 1$ look much smoother and more precise than the result obtained at $t = 40$. This phenomenon is caused by the evolution of particle arrangement over time. At $t = 1$, the Lagrangian particles are distributed evenly at the lattice points. At $t = 40$, the particles have moved along their prescribed trajectories, and their arrangement would appear rather random, especially near the centers of the dipole (Figure 3.2 (b)). Furthermore, the FTLE field at $t = 40$ exhibits a few spots with exceedingly high value. Because some particles are clustered closely together, the initial distances between pairs of particles are extremely small. Such small perturbation implies a rather large final to initial distance ratio which would result in a large FTLE value. To further illustrate the point, the "hot spots" in the FTLE field in Figure 3.1 are matched with the clusters of tracer particles in Figure 3.2. The FTLE values obtained from the current algorithm are approximated values and they are only evaluated to reveal the locations of the local maxima in the FTLE field. In Figure 3.1, the regions with locally high FTLE values join to form an oval ridge that coincides with the dipole boundary indicated by the streamline plot in Figure 2.1 (a). Therefore, the results confirm that the current algorithm can identify the coherent structures of the flow field accurately.

3.1.1 Comparing the FTLE field: The Norm Method

Furthermore, to set up the experiment for this project, the ideal tracer density should be estimated to precisely display the LCS in the flow field. This problem can be easily resolved by further analysis on the flow over a vortex dipole. Figure 3.3 displays the FTLE field of a vortex

dipole flow deployed with tracers of various densities. By superimposing the theoretical LCS and the calculated FTLE field, Figure 3.3 demonstrates that regions with high FTLE values can be recognized accurately with a wide range of particle densities. Taking the extreme case with particle spacing of 0.4 (which translates to particle density of 6.25), the "patches" of high FTLE value roughly match with the theoretical answer although the algorithm yields rather coarse results.

However, determining the ideal particle density by looking at the FTLE field of the test cases is a rather arbitrary process. If an exact solution to the FTLE field exists, the limit of the resulting FTLE field of the current algorithm as the particle density approach infinite will be

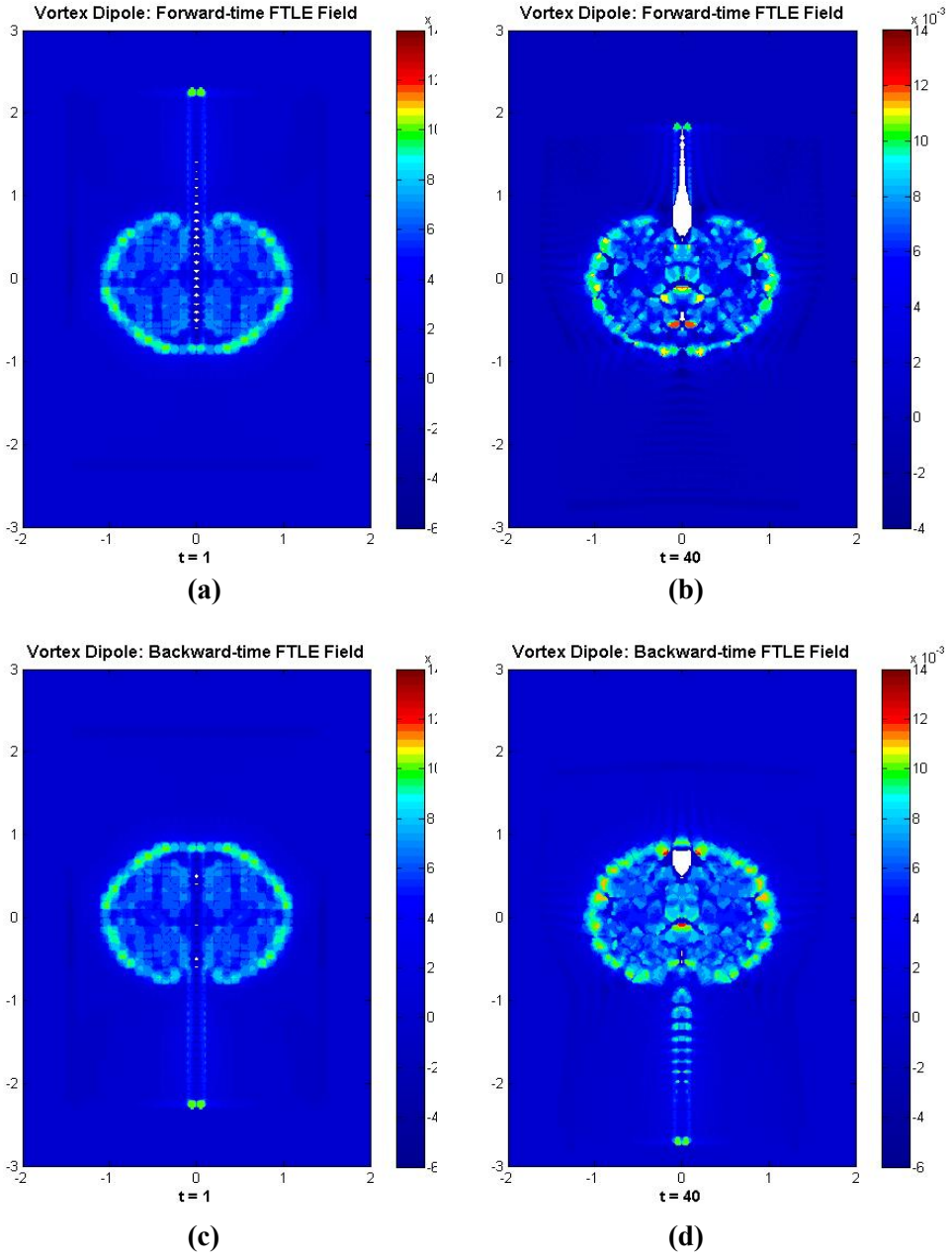

Figure 3.1 The FTLE field of vortex dipole flow:

(a) plots the forward-time FTLE field of the vortex flow at t=1. (b) plots the forward-time FTLE field at t=40.
(c) plots the backward-time FTLE field of the vortex flow at t=1.
(b) plots the backward-time FTLE field at t=40.

The finite time interval the FTLE values are evaluated over is 300 time steps. The tracer particles start at lattice grids with 0.1 unit spacing and have a density of 100 per unit area approximately.

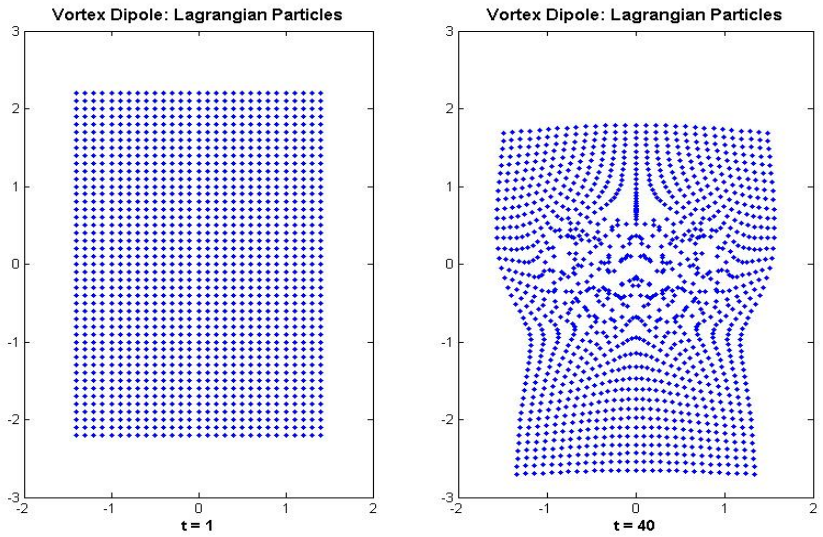

Figure 3.2 These two figures plot the position of the tracer particles moving in a vortex dipole flow at (a) t=1 and (b) t=. The particles starts are initially distributed evenly over a lattice grid, then move along their corresponding trajectories illustrated in Figure 2.1(a).

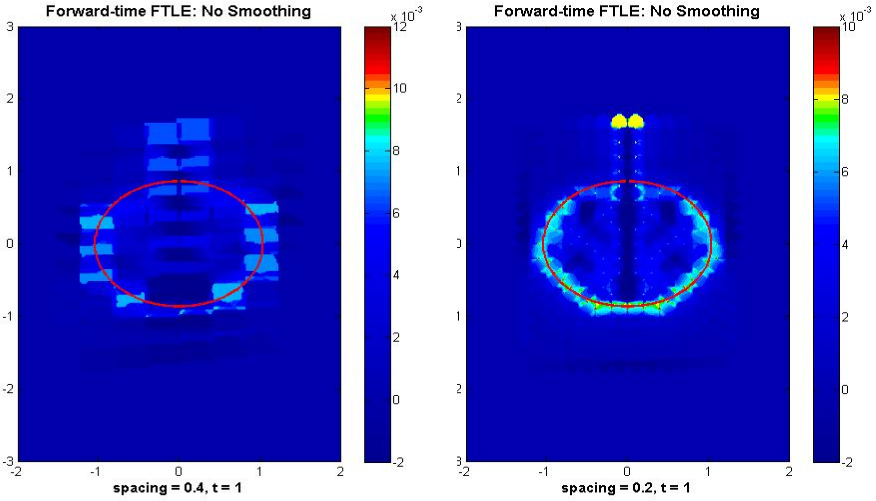

(a) **(b)**

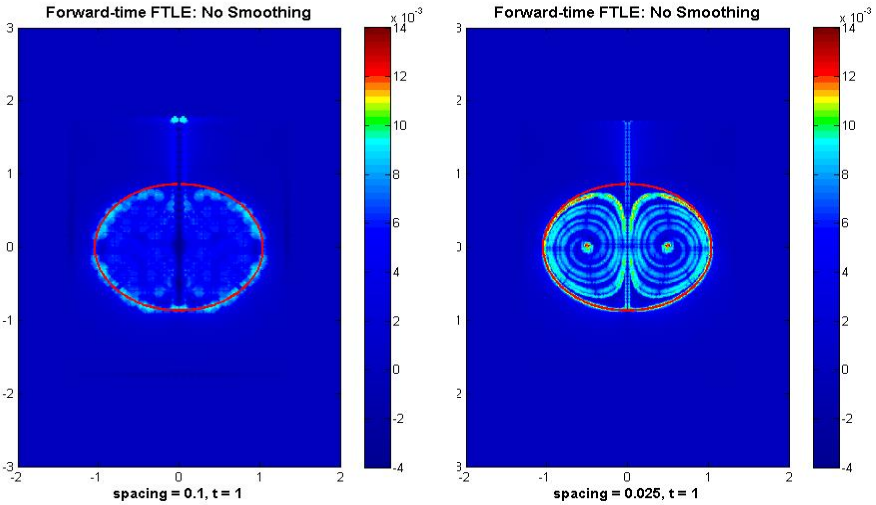

(c) **(d)**

Figure 3.3 Forward-time FTLE plot for vortex dipole flow with different tracer densities at t=1. The integration time interval is 300. The actual solution to the LCS in the flow is plotted in red for all different cases.

(a) spacing=0.4, density=6.25 .
(b) spacing=0.2, density =25.
(c) spacing=0.1, density=100.
(d) spacing=0.025, density=1600.

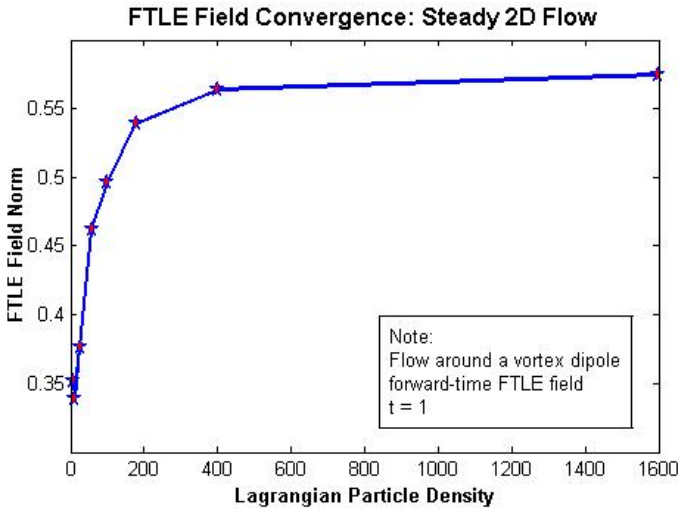

Figure 3.4 The norm of the FTLE field plotted against the particle density. The tested data points are plotted in red stars and connected by blue segments. As the particle density increases, the norm of the FTLE field will reach an equilibrium value.

extremely close to the solution. To assess the effect of tracer density on the FTLE field, we developed a method to compare the FTLE field of different test cases quantitatively: The value matrix of the FTLE field computed from each test case is resized into a n-dimensional vector $\mathbf{v} = v_i = (v_1\ v_2 \dots v_i \dots v_n)$, and the norm of the row vector is calculated from the following equation: $\text{norm}(\mathbf{v}) = (\Sigma_1^n v_i^2)^{1/2}$. We can deduce from this formula that if the entry values of two vectors are very close to each other, the norm of the two vectors will be very close also. Figure 3.4 plots the FTLE field norm of each test case against the particle density. As the plot shows, the norm of the FTLE field quickly approaches an equilibrium value as the particle density increases.

Figure 3.3 and 3.4 demonstrate a wide range of results that can be obtained from the current algorithm. Although we wish to see the extremely precise answer shown in Figure 3.3(d), the number of tracers suggested in this case (~40,000) is very difficult to attain, and the increased number of tracers will prolong the overall computation and possibly interfere the flow. Using excessive number of tracers would also be hard for the particle tracking algorithm to track each tracer accurately. Since our objective is to visualize the LCS in the flow field, we only need to clearly identify the locations of the local maxima. According to Figure 3.3 and 3.4, a particle density around 150 per unit area is sufficient to extract the desired result.

Furthermore, investigations on other vital elements of the experiment, such as the grid resolution, the time step size, and the tracking time, are also performed to assess their effect on the output. However, the analysis on these control variables is neglected due to their minimal effect on the output. Specifically, time step size is a very important component in the Eulerian method because it determines the error size of the flow map integration. However, in the current algorithm, the exact location of each tracer particle is measured. As a result, the error due to flow map integration is eliminated and so is the effect of time step size on the output. For the analysis on the grid resolution, because the FTLE fields for the test cases have different

dimensions, the norm method cannot be applied to the results. Although by intuition, a greater grid resolution usually leads to a more precise answer, it adds extra burden on the computation process. Therefore, it is simply a matter of optimization, and the ideal grid resolution would be determined by the time frame and the desired accuracy of the experiment. Moreover, the effect of tracking time on FTLE field for vortex dipole flow is also insignificant because the flow model is steady and the LCS in the flow field are stationary. In contrary, for an unsteady flow, the tracking time heavily influences the output and its effect is further discussed in Chapter 3.3.

Lastly, most of the results demonstrated so far have obtained from a even distribution of tracer particles. Yet the particle placement in a realistic situation would appear rather chaotic. Figure 3.5 shows the FTLE field calculated from a random initial tracer arrangement with particle density of 100 per unit area. Although the result appears less smooth and has many more high FTLE value "hot spots" than the even distribution with the same particle density (Figure 3.3 (a)), it is able to recognize the regions with high FTLE value and reveal the corresponding LCS. Therefore, the final result of the algorithm is insensitive to the initial arrangement of the tracer particle.

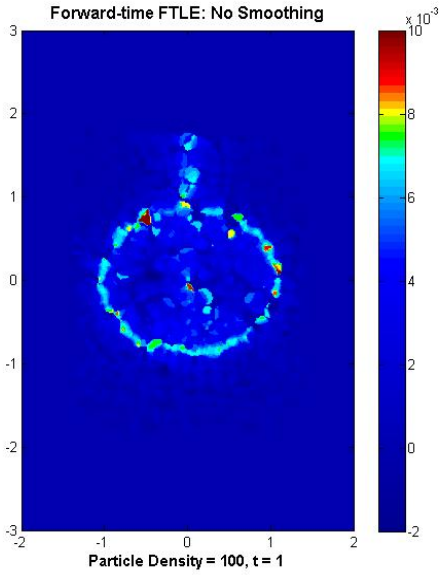

Figure 3.5 Forward-time FTLE field for a vortex dipole flow with random initial tracer distribution.

3.2 Three-dimensional Steady Flow: Hill's Vortex Dipole

Because the current algorithm will be applied to three-dimensional time-series data, it is necessary to test the algorithm on a three-dimensional flow model. As a classic flow model, Hill's vortex sphere naturally becomes the candidate for the test model. In the case illustrated by Figure 3.6, tracer particles are randomly distributed in a rectangular volume at frame 1 ($t = 1$) with the density of 500 particles per unit volume. They then move along their prescribed trajectories based on Equation 2.3 and 2.4. The plots in Figure 3.6 shows the positions of the tracer particles at (a) $t = 1$, (b) $t = 25$, and (c) $t = 51$. According the plot, the particles that start within the vortex sphere are trapped in the sphere; the particles outside the sphere at $t = 1$ will move down stream past the sphere. The surface of the vortex sphere serves as the material surface that separate the flow field into two distinct regions. Therefore, the LCS of this three-dimensional flow model is the surface of the vortex sphere. However, visualizing a three-dimensional FTLE field is a rather challenging task because it is unfeasible to generate a three-dimensional contour plot on a sheet of paper. Nonetheless, in the current algorithm, because the

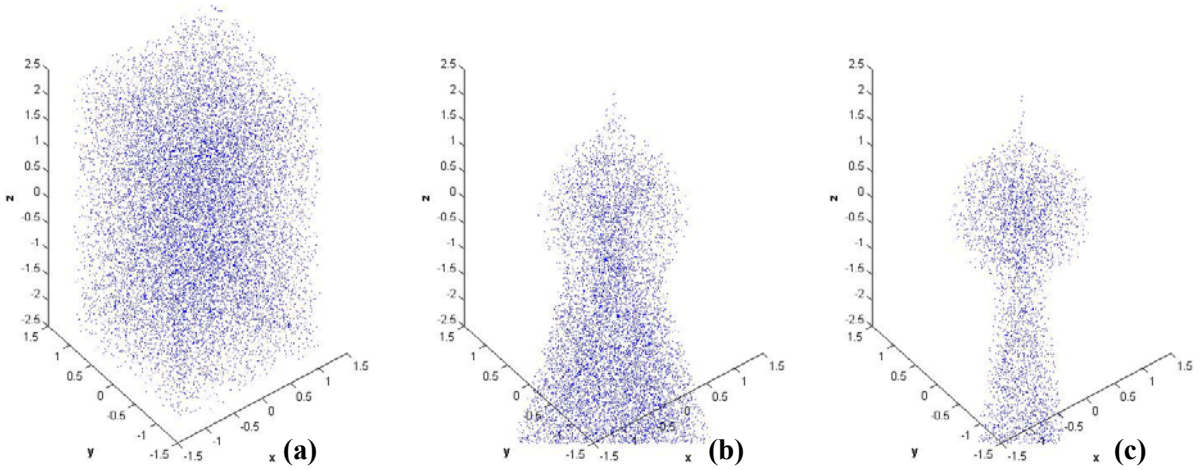

Figure 3.6 These three figures plot the position of the tracer particles moving in a flow pass over Hill's vortex sphere at (a) $t = 1$, (b) $t = 25$, and (c) $t = 51$. The particles starts are initially distributed randomly in a rectangular volume, then move along their prescribed trajectories illustrated in Figure 2.1 (b). The particle density is 500 per unit volume.

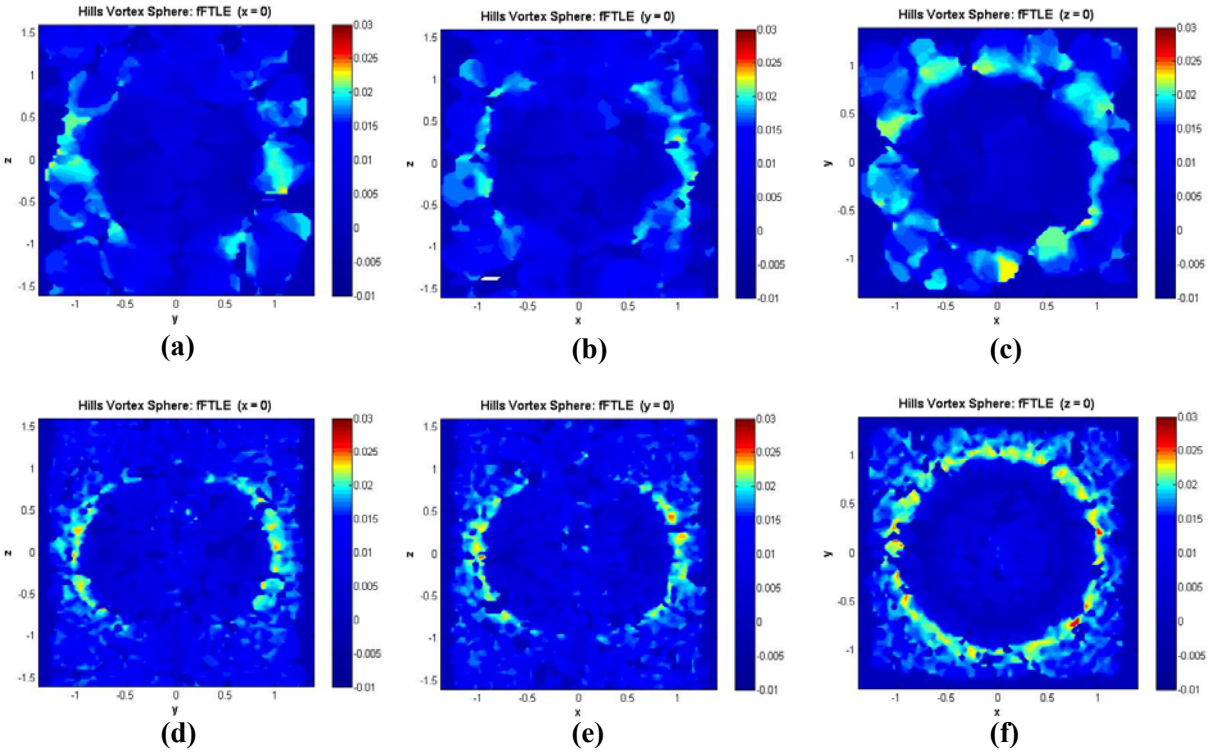

Figure 3.7 Forward-time FTLE plots for Hill's vortex sphere with different tracer densities at $t = 1$. The tracking time interval for all plots is 150. The particle density is 5 per unit volume for figure (a), (b) and (c); the particle density is 50 per unit volume for figure (d), (e) and (f). (a) and (d) show the FTLE field on the *x*-*z* plane; (b) and (e) show the FTLE field on the *y*-*z* plane; (c) and (f) show the FTLE field on the *x*-*y* plane.

FTLE field of the flow field is actually computed over an Eulerian grid (p.11). We can specify a plane parallel to one of the three principal planes ($y = 0$, $x = 0$, and $z = 0$) and plot the FTLE values on that surface. Figure 3.7 shows the forward-time FTLE field of trajectory data with different particle densities (50 and 500 per unit volume) calculated on the x-z, y-z, and x-y plane. The high-value ridges in each of the plots all have a circular outline, which is exactly the intersection between the spherical LCS and the specified plane. Even for the case with very low particle density (Figure 3.7 (a) ~ (c)), one can roughly identify LCS from the plotted FTLE field. Therefore, the results further confirm that the current algorithm can accurately identify the coherent structures of the flow field in three-dimensional domain.

However, from Figure 3.7 (a), (b), (d), and (e), it is not hard to notice that the LCS become discontinuous near the z-axis, and the LCS on the x-z plane and y-z plane look more like two arcs than a circle. According to the velocity field described by Equation 2.3 and 2.4, as r, the distance between the particle position and the z-axis approaches zero, both u_r and u_z become zeros and u_r collapses to zero much faster than u_z does. Thus, the particles near the z-axis will all move vertically with extremely low speed, and the trajectory divergence between any two particles near the z-axis will not be great enough to induce any high-FTLE-valued ridge. This conclusion is further confirmed in Figure 3.7 (c) and (f), where the LCS on the x-y plane is a complete circle and FTLE value approaches zero near the center ($x = 0$, $y = 0$).

According to the two-dimensional flow model, the ideal particle density is between 100 and 150 per unit area. If we extrapolate the result from the two-dimensional flow model to the third dimension, then a particle density from 1000 to 2000 particles per unit volume will yield a desirable result. This implies the minimum number of tracers required to run the experiment is approximately 80,000, which is nearly an astronomical number for an experiment for small scale flow measurement. As mentioned in Chapter 3.1, such large number of particles is hard to attain; it will prolong the computation and possibly affect the fluid flow. Therefore, various particle densities that are more realistic to achieve in an experiment are tested. From Figure 3.7, we can see that the particle density of 500 is adequate to locate the LCS accurately. Furthermore, the norm method is performed on the test cases to assess the effect of tracer particle density. Figure 3.8 provides the plot of the FTLE field norm for each test case versus the particle densities, and the plot also suggests that a particle density between 500 and 1000 will give a plausible estimate to the exact FTLE field.

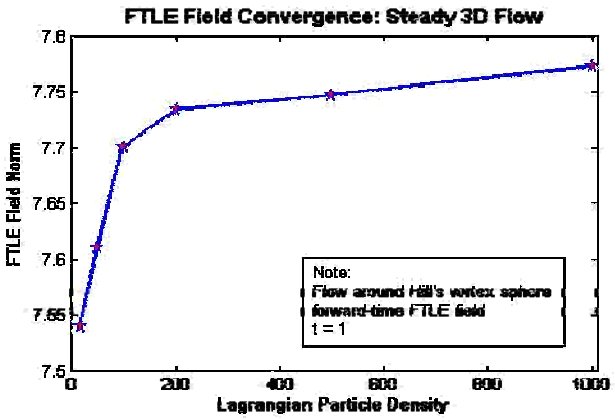

Figure 3.8 The norm of the FTLE field plotted against the particle density. The tested data points are plotted in star and connected by blue segments. As the particle density increases, the norm of the FTLE field will reach an equilibrium value.

3.3 Two-dimensional Unsteady Flow: Flow around Jellyfish

The Lagrangian method has shown promising results in analytical models of steady flows in both two and three dimensions. However, the type of flow expected in an experiment of animal swimming measurement is rather unsteady and unpredictable. Also, there has not been a developed method that can analytically determine the LCS around a swimming animal. Since FTLE field calculation on a three-dimensional time-series data has never been accomplished, verifying the algorithm with three-dimensional experimental data seems unfeasible. Nonetheless, the Biological Propulsion Lab at Caltech has used DPIV to measure the two-dimensional velocity field around a swimming jellyfish. The LCS around a swimming jellyfish has also been extracted from the velocity data via the Eulerian method. Therefore, the two-dimensional PDIV data is tested in our current algorithm, and the results obtained by the Eulerian method will be used to validate the current algorithm.

In order to simulate a Lagrangian approach to the experiment, tracer particles are seeded in the velocity field, and their trajectories are integrated over a finite time interval to resemble a

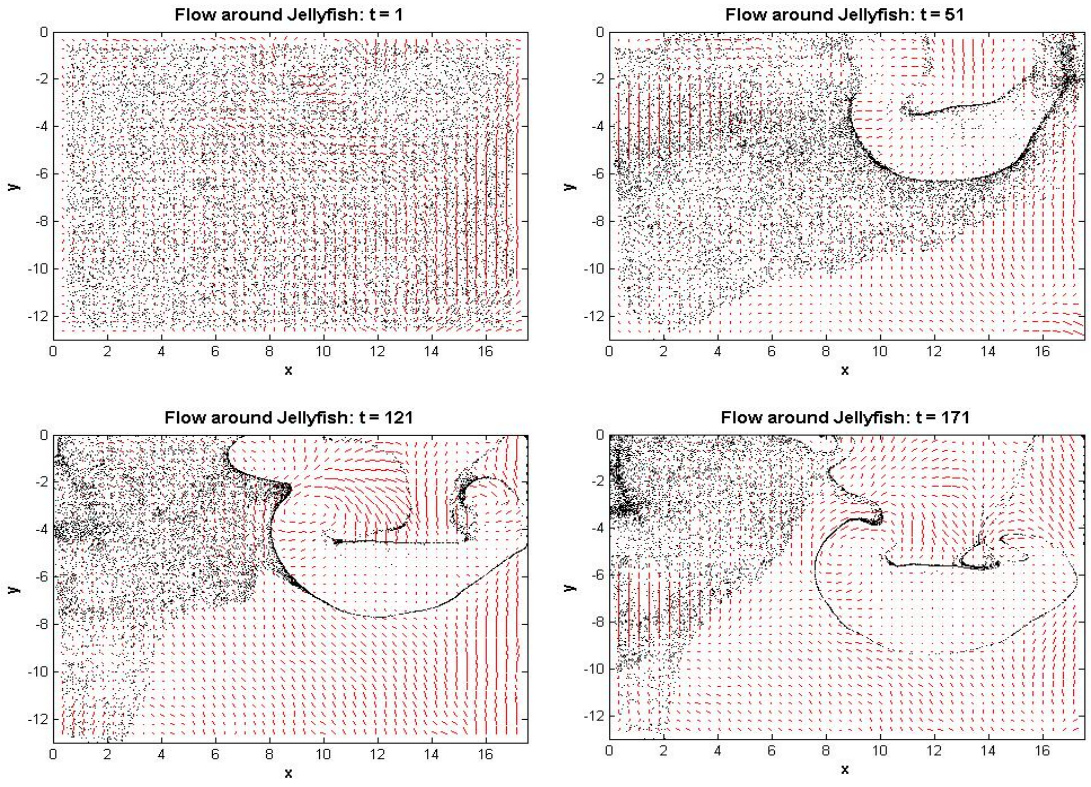

Figure 3.9 These figures plot the velocity field (red vectors) from the previous PDIV measurement on a swimming jellyfish at $t = 1$, $t = 51$, $t = 101$, and $t = 151$. During the experiment, a moon jellyfish enters from the upper right hand side of the field and propels downward. The tracer particles are seeded in the velocity field, and they are marked as black dots in these plots. The tracers have a density of 30 particles per unit.

time-series data. Figure 3.9 shows the plots for the positions of the tracer particles at various time frames. The velocity field at each frame is also plotted on the same figures. In this simulated experiment, particles with density of 30 per unit area are seeded around a jellyfish, and the jellyfish propels toward the bottom the domain by generating vortices underneath its body. During the process, the silhouette of the jellyfish becomes more and more visible as the particles are pulled towards the jellyfish and adhere to the bell due to the viscous effect of water. The layer of particles does not only outline the bell of jellyfish, but also the wake beneath it. Evidently, these wakes form a fluid-fluid boundary, where particles cannot pass through, and this observation is confirmed in the FTLE field plots in Figure 3.10, where LCS are identified. Figure 3.10 (a) and (b) plot the forward-time FTLE field at $t = 51$ and $t = 51$, and Figure 3.10 (c) and (d) plot the back-ward FTLE field at $t = 121$ and $t = 171$. The invisible boundary where tracer particles adhere to is revealed as the reverse-time LCS (*r*LCS) (Figure 3.10 (c) and (d)) because these particles are pulled onto the wake-formed boundary by the swimming jellyfish, and by definition (pg. 3), *r*LCS are the separatrices that attract surrounding trajectories. At later time frames of the experiment (i.e. $t = 121$ and $t = 171$), the flow under the belly of the jellyfish is actually enclosed by the *r*LCS. Since particles cannot pass through LCS, jellyfish generate vortices beneath them not only to help with their movement, but also trap the preys into the

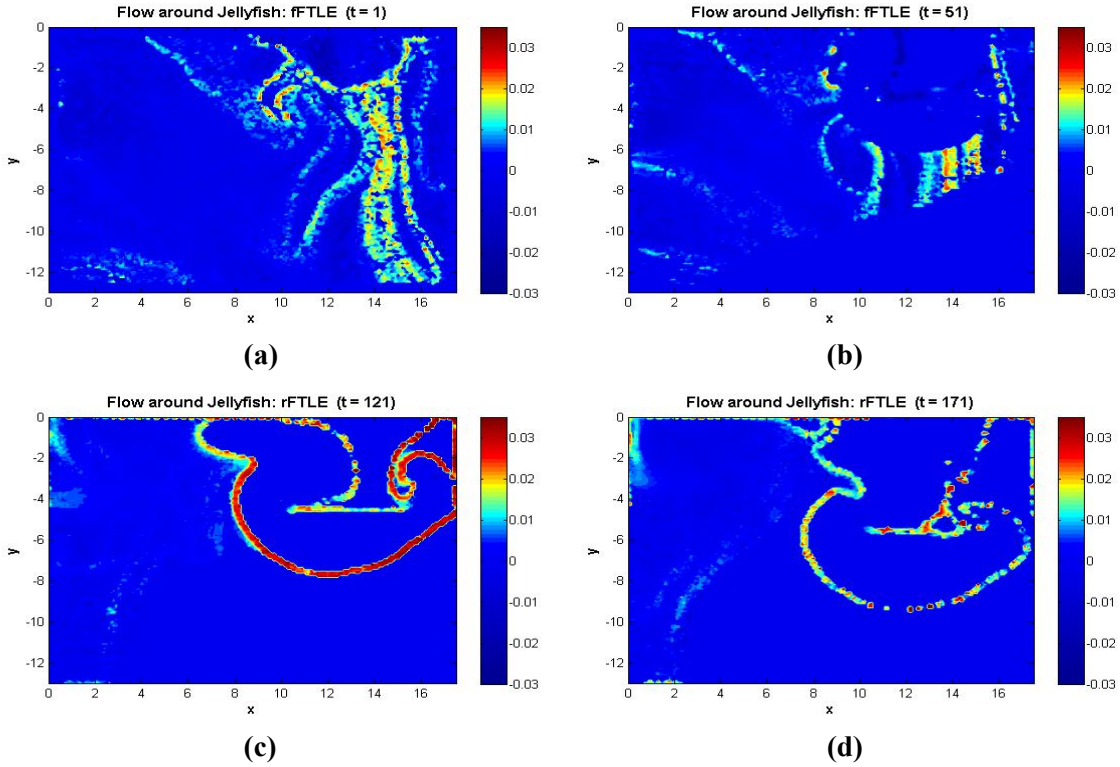

Figure 3.10 These plots illustrate the FTLE field of the flow around a swimming jellyfish. The tracking time interval for all plots is 120, and the tracer density is at 30 particle per unit area. (a) and (b) show the forward-time FTLE field at $t = 1$ and $t = 51$; (c) and (d) show the backward-time FTLE field at t = 121 and t = 171. A total of 200 frames of data are available.

region within the reach of their tentacles. In addition to the *r*LCS, Figure (a) and (b) show the forward-time LCS (*f*LCS) around the jellyfish. In fact, the *f*LCS reveal a unique feature of the flow around jellyfish—lobes. They are the long and narrow channels above the bell of the jellyfish that guide material into the region enclosed by the *r*LCS. As a result, the tracer particles are pulled towards the bell through the paths created by the lobes. As a matter of fact, similar results can be found in previous works, such as Peng et al. (2007) and Shadden et al. (2006), using the Eulerian method, which further confirms the accuracy of our results.

However, the *f*FTLE field plots expose a major disadvantage of the Lagrangian method. Because the FTLE value at each grid point highly depends on the presence of the nearby tracer particles. The region with no particles floating around will simply return zero for the FTLE value. Although *r*LCS are always visible because they attract surrounding particles, *f*LCS are much more difficult to identify since they repel nearby trajectories. As shown in Figure 3.10 (b), the lobes are simply curtailed because the particles that are originally on the bottom right of the domain are pulled towards the jellyfish. In a real experiment, the jellyfish will be swimming when the sensors start collecting data. The initial placement of the particles will not be as uniformly distributed as the particles in the simulation due to the vortices constantly coming off the edge of the bell. This phenomenon presents a challenge to the design of the experiment and will be an excellent subject for future study.

3.3.1 Particle Density Normalization

Although Chapter 3.1.1 has extensively discussed the effect of particle density in a two-dimensional flow, the ideal density obtained from the simulations cannot be directly applied to the experiment. A conventional dimensionaless scaling parameter such as the Reynolds number cannot be used since potential flows are inviscid. However, the result obtained from two-dimensional flow model can be roughly translated into experimental study via a normalization method. According to the streamline plot of the vortex dipole flow in Figure 2.1 (a), the diameter of the oval vortex shell (L_{vortex}) is approximately 2. Since the shape of the region enclosed by the bell and the wake-formed boundary of a jellyfish roughly resembles an oval shape (Figure 3.10 (d)) and the width of the shape (L_{jelly}) is about 6. If we multiply the particle densities from both types of flows by the square of the corresponding characteristic lengths, then the resulting densities should be a set of normalized values (ρ_{norm}). Hence,

$$\rho_{norm} = \rho_{vortex} L_{vortex}^2 = \rho_{jelly} L_{jelly}^2 , \tag{3.1}$$

where the normalized particle density can be defined as the number of particles per region of interest. The variations of Equation 3.1 will allow us to calculate the ideal density for the experiment from the density for the vortex dipole flow:

$$\rho_{jelly} = \rho_{vortex} \left(\frac{L_{vortex}}{L_{jelly}} \right)^2 = \frac{\rho_{norm}}{L_{jelly}^2} . \tag{3.2}$$

For example, a particle density of 50 in the vortex dipole flow should be equivalent to 5.6 particles per unit area in the flow around a jellyfish. If we inspect the FTLE plot in Figure 3.3(b) (50 particles per unit area) with Figure 3.11(a) (5 particles per unit area), the clarity and precision of the LCS highlighted in the respective flow fields are roughly equal due to the same normalized particle density. Figure 3.12 (a) plots the FTLE field norm for the flow around a jellyfish versus the particle densities; Figure 3.12 (b) plots the normalized FTLE field against the normalized particle density for both vortex dipole flow and flow around a jellyfish. The FTLE field norm is normalized by dividing it by the predicted equilibrium value obtained from exponential fitting. The obvious similarity between the two curves further verified the proposed theory.

However, the LCS in the flow around a swimming animal are much more intricate and require much more precision than the simple oval-shaped LCS in the vortex flow. In Figure 3.11,

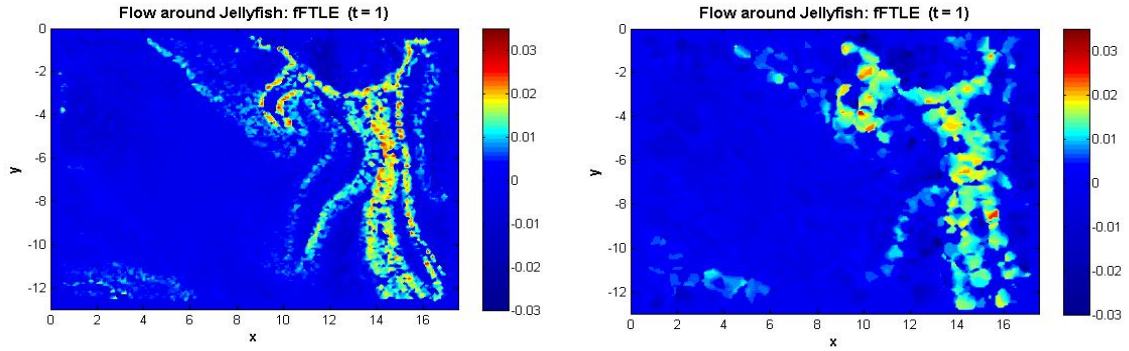

Figure 3.11 These plots illustrate the forward-time FTLE field of the flow around a swimming jellyfish at $t = 1$. The tracking time interval for all plots is 120, and the tracer densities are at (a) 30 particle per unit area, and (b) 5 particles per unit area.

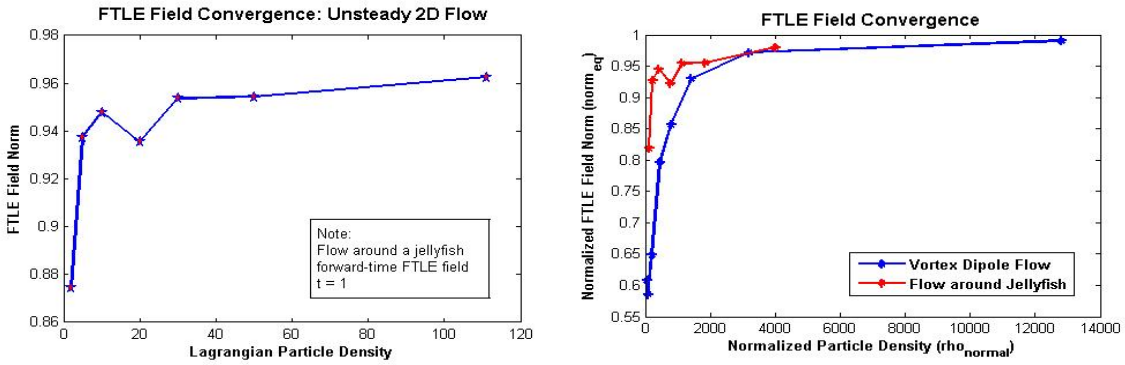

Figure 3.12 FTLE field norms plotted against the tracer particle densities. (a) shows the forward-time FTLE field versus the particle density for the flow field at $t = 1$; (b) plots the normalized FTLE field norm against the normalized particle density.

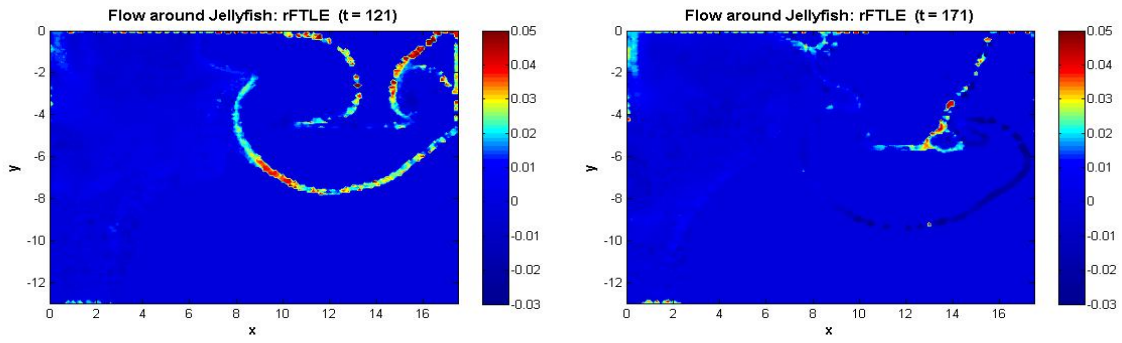

Figure 3.13 These plots illustrate the backward-time FTLE field of the flow around a swimming jellyfish with a short tracking time length of 70 frames at (a) $t = 121$, and (b) $t = 171$. Compare them with Figure 3.10 (c) and (d).

the lobes extending from the top of the bell can be clearly identified in plot (b) but are smeared into one thick strip in plot (a), which has a much lower density. Therefore, in order to ensure accuracy of the flow measurement, a particle density higher than the prediction based on the analytical flow model should be considered for the experimental data collection.

Lastly, the effect of tracking time (or integration length in the Eulerian method) on the FTLE field is extensively investigated for the two-dimensional unsteady flows. According to Equation 2.11, the tracking time appears in the denominator of the expression that evaluates the FTLE at each grid point. Since the logarithm of the trajectory divergence is divided by the tracking time, which outgrows a logarithmic function, the longer the tracking time is, the less the resulting FTLE value at every grid will be. Therefore, the increased tracking time will scale down the FTLE field norm value. The norm method, hence, is no longer valid to provide the quantitative assessment of the effect of a tracking time on the output. Nevertheless, qualitative comparisons between different FTLE field plots are legitimate to provide additional insights on the effect of tracking time on the results. Figure 3.13 (a) (b) and Figure 3.10 (c) (d) illustrate the FTLE field computed at the same time frames but with different tracking time. By observation, a longer tracking time will result in a more precise and accurate measurement on the LCS location in the flow. In Figure 3.13 (a), the high value ridges in the FTLE field does not extend as far down-stream as the *r*LCS of the other case, where the LCS actually encloses a region beneath the jellfish. In Figure 3.13 (b), when tracking particles backward in time, the portion of the separatix on the bell surface actually becomes a low-valued FTLE trench. Since the particles are tracked for such a short time ($T = 70$), the particles around the low-FTLE-valued may have adhered to the top surface of the jellyfish. As the particles are washed away from each other by the stream of water pulled down by the jellyfish, their trajectories will diverge and result in the low value trench in the FTLE field. Conclusively, a longer tracking time will ensure a much more thorough LCS extraction in the flow field.

Chapter 4

Conclusion and Future Work

Using an innovative analytical tool, the Lagrangian coherent structures for different types of vortex flows (both steady analytical models and unsteady experimental data) are measured and analyzed by tracking Lagrangian particles in the flow field. Through parameter variations such as the tracer particle density and the tracking time length, the results obtained by the presented algorithm are verified by either theoretical solutions or results from previous works. Although the LCS extracted by the Lagrangian method may not be as precise as similar results from previous works such as Shadden et al. (2005) and Peng et al. (2007), the Lagrangian method significantly simplifies the computation without sacrificing the overall accuracy of the results because it avoids the lengthy integration of the entire flow map. The substantial curtail of the computational cost allows the possibility of performing LCS extraction on three-dimensional time-series data within a reasonable time frame by using a personal computer. Also, the generic nature of the algorithm allows us to perform LCS extraction on any two or three-dimensional time-series data, not just fluid flow measurements.

However, the Lagrangian method does present a few concerns on the design of the experiment on three-dimensional flow measurement currently conducted by the research group led by Professor John Dabiri. First, the results presented in the thesis suggest a normalized particle density of about 7000 per unit volume is required to achieve a desirable output. Using such large number of particles in the experiment will prolong computation, raise ambiguity for particle tracking, and even distort the entire fluid flow. The analysis on the presented algorithm also suggests that the tracking time will have to be sufficiently long to yield plausible results. Yet, a great portion of the experimental measurements are obtained as auxiliary data that keep tracks of the particle trajectories and only a small portion of the data are used to visualize the LCS.

Nonetheless, the current algorithm has shown promising results in simulations. Further measurements on three-dimensional flows around swimming animals, such as the moon jellyfish, will be performed in the near future to continue our quest to understanding the dynamics of animal swimming. This will motivate further investigations on vortex flows, the dominant flow pattern for biological propulsion, which will influence the development of new locomotion systems.

Acknowledgements

First and foremost, I would like to thank my thesis advisor, Professor John Dabiri from GALCIT, for his invaluable guidance over the course of the year. His support and confidence in me motivates me to accomplish this challenging task. I also want to thank Jeff Peng from the Biological Propulsion lab for his technical assistance. My further appreciation goes to Professor Richard Murray for providing such a great opportunity for undergraduate students to perform rigorous research. My thanks also go to Brandt Belson, Chris Schantz, Kevin Dick, and many others who have helped me during the course of the thesis project.

Zhonglin Zhang
June 6th, 2008

Bibliography

[1] Anderson E.J., McGillis W.R., Grosenbaugh M.A. 2001, *The boundary layer of swimming fish*. J Exp Biol 204:81–102

[2] Eldredge J. D., Colonius T., and A. Leonard. 2002, *A vortex particle method for two-dimensional compressible flow*. J. Comput. Phys, 179:371-399.

[3] Green M.A., Rowley C.W., Haller G. 2006, *Detection of Lagrangian coherent structures in 3D turbulence*. J Fluid Mech 572:111–120.

[4] Haller G. 2001, *Distinguished material surfaces and coherent structures in three-dimensional fluid flows*. Physica D 149:248–277.

[5] Haller G. 2000, *Finding finite-time invariant manifolds in two-dimensional velocity fields*. Chaos 10:99–108.

[6] Mackenzie D. 2007, *Turbulence: Finding order in chaos*, New Scientist, December 01, issue.

[7] Lamb H. 1932, *Hydrodynamics*. Dover, New York.

[8] Peng J., Dabiri J.O. 2007, *A potential-flow, deformable-body model for fluid-structure interactions with compact vorticity: application to animal swimming measurements*. Exp Fluids DOI 10.1007

[9] Pereira F., Gharib M. 2002, *Defocusing digital particle image velocimetry and the three-dimensional characterization of two-phase flows.* Meas. Sci. Technol. 13 683–694.

[10] Rogers S., Waigh T., Zhao X., and Lu J. 2007, *Precise particle tracking against a complicated background: polynomial fitting with Gaussian weight*. Phys. Biol. 4 220–227.

[11] Shadden S.C., Dabiri J.O., Marsden J.E. 2006, *Lagrangian analysis of entrained and detrained fluid in vortex rings*. Phys Fluids 18:047105.

[12] Shadden S.C., Lekien F., Marsden J.E. 2005, *Definition and properties of Lagrangian coherent structures from finite–time Lyapunov exponents in two-dimensional aperiodic flows*. Physica D 212:271–304.

[13] Strogatz, S. H. 1994, *Nonlinear dynamics and chaos: With applications to physics, biology, chemistry, and engineering*. Reading, MA: Perseus Books, Cambridge MA.

[14] Verhulst F. 1996, *Nonlinear Differential Equations and Dynamical Systems*, 2nd Ed. Springer-Verlag, New York.